



HAL
open science

A Direct Method for the Assessment of Cohesive Zone Models for Thin Adhesive Layers Loaded in Mode I, Mode II, and Mixed-Mode I/II

Eric Paroissien, Frederic Lachaud, Joseph Morlier, S. Schwartz

► To cite this version:

Eric Paroissien, Frederic Lachaud, Joseph Morlier, S. Schwartz. A Direct Method for the Assessment of Cohesive Zone Models for Thin Adhesive Layers Loaded in Mode I, Mode II, and Mixed-Mode I/II. *Reviews of Adhesion and Adhesives*, 2018, 10.7569/RAA.2018.097301 . hal-01788130

HAL Id: hal-01788130

<https://hal.science/hal-01788130>

Submitted on 8 May 2018

HAL is a multi-disciplinary open access archive for the deposit and dissemination of scientific research documents, whether they are published or not. The documents may come from teaching and research institutions in France or abroad, or from public or private research centers.

L'archive ouverte pluridisciplinaire **HAL**, est destinée au dépôt et à la diffusion de documents scientifiques de niveau recherche, publiés ou non, émanant des établissements d'enseignement et de recherche français ou étrangers, des laboratoires publics ou privés.



A Direct Method for the Assessment of Cohesive Zone Models for Thin Adhesive Layers Loaded in Mode I, Mode II, and Mixed-Mode I/II

E. Paroissien^{1*}, F. Lachaud¹, J. Morlier¹ and S. Schwartz²

¹Institut Clément Ader (ICA), Université de Toulouse, CNRS, INSA, ISAE-SUPAERO, Mines Albi, UPS, 3 Rue Caroline Aigle, 31400 Toulouse, France

²SOGETI High Tech, R&D Dpt., Aeropark, 3 Chemin de Laporte, 31100 Toulouse, France

Abstract: In the context of increasing the strength-to-mass ratio of lightweight structures, the adhesively bonded joining technology appears to be an attractive solution. Nevertheless, the adhesive bonding method is important when the structural integrity of joints has to be ensured. In the literature, the cohesive zone models (CZMs) are shown to be able to predict both the static and fatigue strengths of adhesively bonded joints. The strength prediction is dependent on material laws and associated material parameters, characterizing the bondline behaviour mainly under pure mode I, mode II and mixed-mode I/II. The characterization methods are thus crucial. This paper aims at assessing the capabilities to identify the parameters of a particular CZM for both the inverse method, based on the energy balance associated with the path independent J-integral, and of a direct method described in this present work. The particular CZM has a classical shape based on the definition of a bilinear law for each of both pure modes, associated with pure mode interaction energy laws for initiation and propagation under mixed-mode I/II. The methodology used in this paper is based on a numerical test campaign only, involving the macro-element (ME) technique. A new approach for the fast formulation and implementation of ME modelling of two bonded beams is described.

Keywords: Adhesively bonded joint, cohesive zone model, macro-element, mode I, mode II, mixed-mode I/II, inverse method, direct method

1 Introduction

In the frame of structural design, the proper choice of joining technology is decisive for guaranteeing the integrity of the manufactured structure. The mechanical

*Corresponding author: eric.paroissien@isae-superaero.fr

DOI: 10.7569/RAA.2018.097301



fastening, such as riveting or screwing, appears to be the reliable solution for the designers. Nevertheless, alone or in combination with the mechanical fastening, the adhesive bonding technology may offer significantly improved mechanical performance in terms of stiffness, static strength and fatigue strength [1–2]. This higher level of mechanical performance allows for the design of lighter joints. In other words, the adhesive bonding offers the possibility to reduce the structural mass while ensuring the mechanical strength. The optimization of the strength-to-mass ratio is a challenge for several industrial sectors, such as aerospace, automotive, rail or naval transport industries. But, the reduction of structural mass makes sense only if the structural integrity is ensured. So to obtain the benefit from the adhesive bonding in view of mass reduction, it is required to be able to predict the strength of bonded joints.

The strength prediction consists in the comparison of computed strength criteria with allowable design values. The strength criteria could be based on theoretical, empirical, semi-empirical investigations and possibly including in-service feedback. The stress analysis allows for the computation of input data, necessary for the assessment of strength criteria. The experimental characterization allows then for the definition of allowable design values as well as of mechanical behavior to be used as input data for the mechanical analysis. As highlighted in [3], the strength of a joining system at the macroscale depends on the experimental test specimen and procedure used. According to recent literature [4–8] the cohesive zone model (CZM) appears to be one of the most suitable approaches that is able to model both the static and the fatigue behaviors of adhesive joints. A CZM offers thus the possibility to experimentally investigate both local and global mechanical behaviors. Based on Damage Mechanics and Fracture Mechanics, the CZM enables a diagnostic of the current state of the adhesive damage along the overlap. The damage associated with micro-cracks and/or voids coalescence results in a progressive degradation of the material stiffness before failure. Contrary to approaches based on Fracture Mechanics, the CZM does not require the hypothesis of the existence of an initial flaw. The localization of critical sites is an output of CZM-based approaches.

The characterization of CZM parameters makes use of a pre-cracked bonded overlap specimen loaded under various loadings, which are classically used in the frame of Fracture Mechanics.

Indeed, the end notched flexure (ENF) and double cantilever beam (DCB) test configurations are most frequently used for characterizing the CZM parameters of the adhesive employed in a thin adhesive layer loaded in pure mode I and pure mode II [7]. The characterization under mixed-mode I/II loading through mixed mode cantilever beam (MCB) and mixed mode bending (MMB) test configurations offers the possibility to subject the adhesive layer to a wide range of mixed-mode ratios while almost keeping the same experimental settings [9–13].

To characterize the CZM parameters, the *inverse method* based on the computation of the path independent J-integral [15] along a closed contour of specifically

designed specimens has been suggested [12-13,15-20]. The inverse method is based on experimental measurements of relative displacements at the crack tip of the bonded interface as a function of the reaction force. The use of the classical model of a beam on an elastic foundation allows for a simple computation of the J-integral and thus for an assessment of the CZM. Nevertheless, it suffers from some limitations mainly due to the hypotheses on which the J-integral is defined. A *direct method* has been previously suggested in [21]. Similarly to the inverse method, it makes use of both the experimental measurements of the displacement field at the bonded interface crack tip and of the model of beam on an elastic foundation. It allows for the characterization of CZM parameters assuming sufficiently accurate experimental measurements.

This paper aims at assessing the capabilities to identify the parameters of a CZM by the inverse method and the direct method. The CZM selected in this paper has a classical shape, based on the definition of a bilinear law for each of the two pure modes, associated with pure mode interaction energy laws for initiation and propagation under mixed-mode I/II. The methodology is based on a numerical test campaign performed only on the MCB test configuration. In other words, numerical tests are employed instead of experimental tests to evaluate both characterization methods. The numerical analysis uses the macro-element (ME) technique [22–24], through a home-made computer code implemented on SCILAB. This technique has already been successfully assessed against the Finite Element (FE) analysis in a similar context [21, 23–24]. Moreover, a new approach for an easy and fast implementation of the ME technique for the modelling of a bonded overlap is provided.

2 Numerical Test Campaign

2.1 Test Configuration

In the frame of the numerical test campaign presented in this paper, the MCB test configuration has been selected. It has been suggested by Högberg and Stigh [12, 13]. Similarly to the DCB test configuration, the loading consists in a pair of forces (termed F), being of the same magnitude but in opposite directions. Nevertheless, the action direction of the pair of forces is defined by an angle α , which allows for the adhesive layer to be subjected to pure mode I, pure mode II and mixed-mode I/II (see Figure 1). In this paper, contrary to the MCB test configuration described in [13], the two forces are not applied at the middle plane of the specimen but at neutral lines of each adherend. This MCB test configuration with $\alpha = \pi/2$ corresponds to a DCB test configuration, while it leads with $\alpha = 0$ to zero peel stress at the crack tip where the CZM parameters are measured.

The selected specimen design, including geometrical and material parameters, corresponds to the one described by Högberg and Stigh [13]. The crack length $a=0$

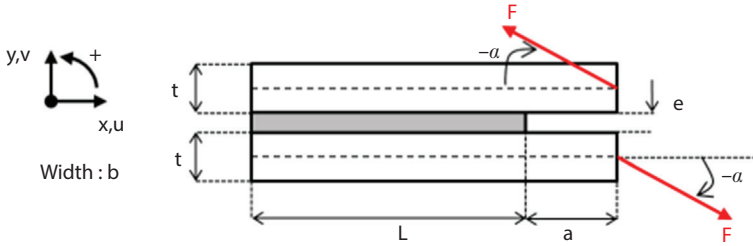


Figure 1 MCB test configuration considered in this paper and the definitions of geometrical parameters.

Table 1 Geometrical parameters of the MCB specimen [14].

a in mm	b in mm	e in mm	t in mm	L in mm
0	4	0.2	8	100

is then chosen (see Figure 1). The geometrical parameters are provided in Table 1 in conjunction with Figure 1.

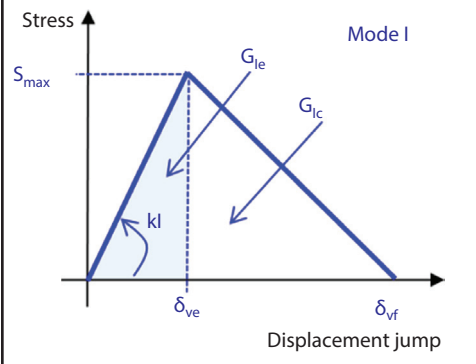
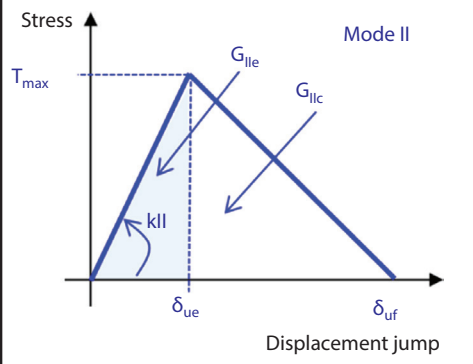
The adherends are made of steel with a Young’s modulus $E = 200 \text{ GPa}$ and a Poisson’s ratio $\nu = 0.3$. The design is such that the adherends will remain in their linear elastic domain. The adhesive is assumed to have a classical bilinear damage evolution law following [25], involving interaction energy laws for both initiation and propagation under mixed-mode:

$$\begin{cases} \left(\frac{G_I}{G_{Ie}}\right)^n + \left(\frac{G_{II}}{G_{IIe}}\right)^n = 1 \\ \left(\frac{G_I}{G_{Ic}}\right)^n + \left(\frac{G_{II}}{G_{IIc}}\right)^n = 1 \end{cases} \quad (1)$$

where n is a material parameter to be identified, G_{Ic} and G_{IIc} are the fracture energies in mode I and mode II, G_{Ie} and G_{IIe} are the elastic strain energies stored in mode I and mode II and G_I and G_{II} are related to the strain energy release rates in mode I and mode II, respectively.

The fracture energies in mode I and mode II and the elastic stiffnesses under peel and shear, termed k_I and k_{II} respectively are the same as those used by Högberg and Stigh [13]. Nevertheless, the adhesive maximal peel and shear stresses, termed S_{max} and T_{max} , are different, to ensure a right energy dissipation during loading [26]. It is indicated that the law by Allix and Ladevèze [25] already includes this condition. It is then chosen to keep the same maximal shear stress $T_{max} = 26 \text{ MPa}$, resulting in a

Table 2 Adhesive material parameters.

			
G_{Ie} in N/mm	G_{Ic} in N/mm	G_{IIe} in N/mm	G_{IIc} in N/mm
0.76	3.128 E-2	3.464 E-2	2.30
δ_{ve} in mm	δ_{vf} in mm	δ_{ue} in mm	δ_{uf} in mm
1.71 E-3	4.15 E-2	7.28 E-3	1.77 E-1
k_I in GPa/mm	S_{max} in MPa	k_{II} in GPa/mm	T_{max} in MPa
21.4	36.6	3.57	26

maximal peel stress $S_{max} = 36.6$ MPa, instead of 20 MPa. The choice of keeping S_{max} to its original value instead of T_{max} does not change qualitatively the results provided in his paper. The material parameters of the adhesive layers are given in Table 2.

2.2 Numerical Analysis

2.2.1 Macro-Element Technique Overview

The numerical analysis is performed using the macro-element (ME) technique for the modelling of bonded overlap [22–24]. This technique has been developed for the simplified stress analysis of hybrid (bolted/bonded) joints [22, 27]. The ME technique is inspired by the Finite Element (FE) method and differs in the sense that the interpolation functions are not assumed, since they take the shape of the solutions of the governing differential equations system. A direct consequence is that only one ME is sufficient to mesh a complete bonded overlap in the frame of a linear stress analysis. The bonded overlap is then modelled by a four-node ME – also called bonded-beams element – the nodes of which are located at the extremities of the overlap on the neutral axes of adherends (see Figure 2). This ME involves 3 degrees of freedom per node or a total of twelve for a 1D-beam analysis.

The main work is thus the formulation of the elementary stiffness matrix of the bonded-beams element. Indeed once the stiffness matrix of the complete structure is assembled from the elementary matrices and the boundary conditions are

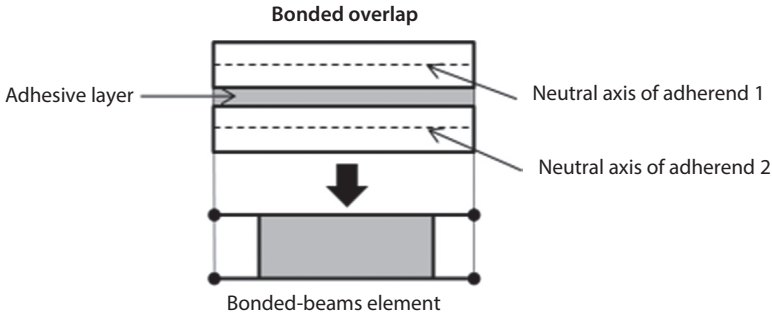


Figure 2 Modelling of a bonded overlap by a bonded-beams element [22–24].

applied, the minimization of the potential energy provides the solution, in terms of distributions along the overlap of adhesives stresses, internal forces and displacements in the adherends.

2.2.2 Hypotheses and Formulation of the Elementary Stiffness Matrix

An approach for the formulation of the stiffness has already been described in detail in previous papers [22–24]. Nevertheless, this approach could be long to set up. In this paper, a new approach is provided for a fast and easy implementation within a mathematical software such as SCILAB for example. Compared with the early approach, the shape of solutions in terms of displacements and internal loads is not provided. Nevertheless, in the frame of nonlinear material analyses such as the one presented in this paper, the bonded overlap has to be meshed in order to locally update the material parameters within an iterative computation procedure (see section 2.2.3). As a result, the displacements and internal loads will be read directly at nodes. Moreover, the following description is useful for the derivation of the direct method.

It is assumed that the thickness of the adhesive is constant along the length Δ of the macro-element. Moreover, the adherends are simulated as linear elastic Euler-Bernoulli laminated beams. The general shape of the constitutive equations for the adherend $j=1,2$ provides the six first differential equations:

$$\left\{ \begin{array}{l} N_j = A_j \frac{du_j}{dx} - B_j \frac{d\theta_j}{dx} \\ M_j = -B_j \frac{du_j}{dx} + D_j \frac{d\theta_j}{dx} \\ \theta_j = \frac{dv_j}{dx} \end{array} \right. \Leftrightarrow \left\{ \begin{array}{l} \frac{du_j}{dx} = \frac{D_j}{\Delta_j} N_j + \frac{B_j}{\Delta_j} M_j \\ \frac{dv_j}{dx} = \theta_j \\ \frac{d\theta_j}{dx} = \frac{B_j}{\Delta_j} N_j + \frac{A_j}{\Delta_j} M_j \end{array} \right. \quad (2)$$

where N_j (M_j) is the normal force (bending moment) of the adherend j and u_j (v_j , θ_j) is the longitudinal displacement (deflection, bending angle) of the adherend j . For the adherend j , A_j represents the extensional stiffness, D_j the bending stiffness and B_j the coupling stiffness and $D_j = A_j D_j - B_j B_j \neq 0$. In this paper, the coupling stiffnesses remain equal to zero and $A_1 = A_2 = Etb$ and $D_1 = D_2 = Et^3b/12$. It is indicated that the Euler-Bernoulli kinematics is employed by Högborg and Stigh in [13].

The adhesive layer is simulated by an infinite number of elastic shear and transverse springs attached at both adherend interfaces. The adhesive shear stress – denoted T – and the adhesive peel stress – denoted S – are then given by:

$$\begin{cases} S = k_I (v_1 - v_2) \\ T = k_{II} (u_2 - u_1 - h_2 \theta_2 - h_1 \theta_1) \end{cases} \quad (3)$$

where h_j is the half thickness of adherend j . In this paper, $h_1 = h_2 = t/2$.

The classical local equilibrium from Goland and Reissner [28] is used and provides the six last differential equations for $j=1,2$ (see Figure 3):

$$\begin{cases} \frac{dN_j}{dx} = (-1)^j bT \\ \frac{dV_j}{dx} = (-1)^{j+1} bS \\ \frac{dM_j}{dx} + V_j + bh_j T = 0 \end{cases} \quad (4)$$

where V_j is the shear force of the adherend j .

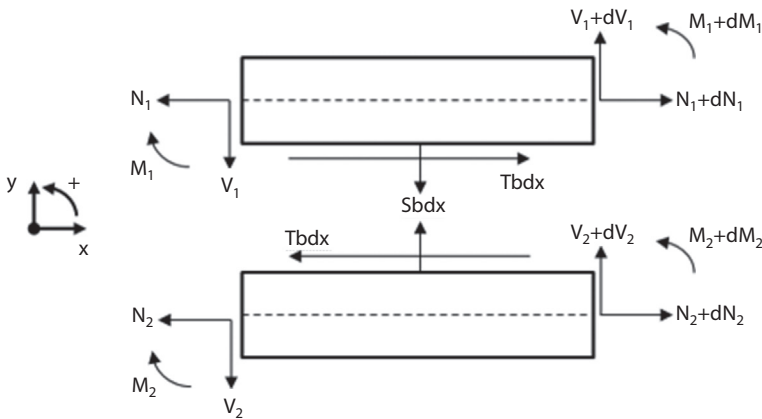


Figure 3 Free-body diagram of infinitesimal elements of the adherend 1 (top) and adherend 2 (bottom).

Considering the local equilibrium equations Eqs. (4), the adhesive stresses are replaced by their expressions as functions of adherend displacements Eqs. (3). In conjunction with Eqs (2), it results in a system of twelve linear first-order ordinary differential equations:

$$\begin{cases}
 \frac{du_1}{dx} = \frac{D_1}{\Delta_1} N_1 + \frac{B_1}{\Delta_1} M_1 \\
 \frac{du_2}{dx} = \frac{D_2}{\Delta_2} N_2 + \frac{B_2}{\Delta_2} M_2 \\
 \frac{dv_1}{dx} = \theta_1 \\
 \frac{dv_2}{dx} = \theta_2 \\
 \frac{d\theta_1}{dx} = \frac{B_1}{\Delta_1} N_1 + \frac{A_1}{\Delta_1} M_1 \\
 \frac{d\theta_2}{dx} = \frac{B_2}{\Delta_2} N_2 + \frac{A_2}{\Delta_2} M_2 \\
 \frac{dN_1}{dx} = bk_{II}u_1 + bk_{II}h_1\theta_1 - bk_{II}u_2 + bk_{II}h_2\theta_2 \\
 \frac{dN_2}{dx} = -bk_{II}u_1 - bk_{II}h_1\theta_1 + bk_{II}u_2 - bk_{II}h_2\theta_2 \\
 \frac{dV_1}{dx} = bk_Iv_1 - bk_Iv_2 \\
 \frac{dV_2}{dx} = -bk_Iv_1 + bk_Iv_2 \\
 \frac{dM_1}{dx} = bh_1k_{II}u_1 + bk_{II}h_1h_1\theta_1 - bh_1k_{II}u_2 + bk_{II}h_1h_2\theta_2 - V_1 \\
 \frac{dM_2}{dx} = bh_2k_{II}u_1 + bk_{II}h_2h_2\theta_1 - bh_2k_{II}u_2 + bk_{II}h_2h_2\theta_2 - V_2
 \end{cases} \tag{5}$$

This system can be written as $\frac{dX}{dx} = AX$ where A is 12×12 matrix with real constant components and the unknown vector X is such that ${}^tX = (u_1 \ u_2 \ v_1 \ v_2 \ \theta_1 \ \theta_2 \ N_1 \ N_2 \ V_1 \ V_2 \ M_1 \ M_2)$. But the elementary stiffness matrix corresponds to the relationship between the vector of nodal forces and the vector of nodal displacements [22–24], such as:



$$\begin{pmatrix} -N_1(0) \\ -N_2(0) \\ N_1(\Delta) \\ N_2(\Delta) \\ -V_1(0) \\ -V_2(0) \\ V_1(\Delta) \\ V_2(\Delta) \\ -M_1(0) \\ -M_2(0) \\ M_1(\Delta) \\ M_2(\Delta) \end{pmatrix} = K_{BBc} \begin{pmatrix} u_1(0) \\ u_2(0) \\ u_1(\Delta) \\ u_2(\Delta) \\ v_1(0) \\ v_2(0) \\ v_1(\Delta) \\ v_2(\Delta) \\ \theta_1(0) \\ \theta_2(0) \\ \theta_1(\Delta) \\ \theta_2(\Delta) \end{pmatrix} \tag{6}$$

The fundamental matrix of A , termed Φ_A , is computed at $x=0$ and $x=\Delta$; using the SCILAB software, the associated command is "expm":

$$\begin{cases} \Phi_A(x=0) = \text{expm}(A.0) \\ \Phi_A(x=\Delta) = \text{expm}(A.\Delta) \end{cases} \tag{7}$$

From these two 12×12 matrices, two matrices M' and N' are extracted. M' (N') is composed of the lines related to the nodal displacements (forces). For each, a first block of six lines and twelve rows comes from $\Phi_A(x=0)$ and the second block of six lines and twelve rows comes from $\Phi_A(x=\Delta)$, such that:

$$\begin{cases} M' = \Phi_U(0, \Delta) = \begin{pmatrix} [\Phi_A(x=0)]_{i=1,2,3,4,5,6 ; j=1:12} \\ [\Phi_A(x=\Delta)]_{i=1,2,3,4,5,6 ; j=1:12} \end{pmatrix} \\ N' = \Phi_F(0, \Delta) = \begin{pmatrix} [\Phi_A(x=0)]_{i=7,8,9,10,11,12 ; j=1:12} \\ [\Phi_A(x=\Delta)]_{i=7,8,9,10,11,12 ; j=1:12} \end{pmatrix} \end{cases} \tag{8}$$

where $i(j)$ indicates the line (row) number.

As K_{BBc} is defined according to $([u_1(0) u_2(0) u_1(\Delta) u_2(\Delta) v_1(0) v_2(0) v_1(\Delta) v_2(\Delta) \theta_1(0) \theta_2(0) \theta_1(\Delta) \theta_2(\Delta)])$, a simple rearrangement of the order of lines of M' is performed to produce the matrix M . Similarly, the matrix N' is subjected to the same operation. In a similar way, the terms related to nodal forces at $x=0$ are multiplied by -1 to follow

the arrangement $([-N_1(0) -N_2(0) N_1(\Delta) N_2(\Delta) -V_1(0) -V_2(0) V_1(\Delta) V_2(\Delta) -M_1(0) -M_2(0) M_1(\Delta) M_2(\Delta)])$. It leads to the definition of the matrix N . The elementary stiffness matrix K_{BBc} is equal to the product of N and the inverse of M [22-24]: $K_{BBc} = N.M^{-1}$.

Even if it is not the topic of this paper, it is obvious that this previous approach can be easily used to develop ME, under different local equilibrium equations (e.g. Hart-Smith [29], Luo and Tong [30]) or under different constitutive equations (e.g. Tsai et al. [31]) and/or including different number of layers of adhesives and adherends (e.g. double lap joint configuration).

2.2.3 Mesh and Boundary Conditions

The bonded overlap is regularly meshed with a parametrical number n_{ME} of bonded-beams elements. One extremity is clamped and the load is applied under displacement (termed H) at the other extremity [24] (see Figure 4). This choice of boundary conditions does not correspond to those experienced during experimental tests [12]. However, it is necessary to prescribe relevant degrees of freedom to run any analysis. In view of the application of the inverse method, it is mandatory that the adhesive layer does not deform at the joint extremity where the load is not applied. Clamping conditions avoid both peel and shear deformations. The inverse and direct methods are then applied by taking into account these boundary conditions (see section 3.1).

The results are not presented in this paper but a study on the influence of mesh size up to a maximal mesh density of twenty MEs per mm was performed under a pure linear elastic analysis under pure mode I ($\alpha = \pi/2$). The conclusions are that (i) the original approach and the present approach for the formulation of the elementary stiffness matrix of ME provides exactly the same results, and (ii) the computed reaction as well as the adhesive peak stresses do not vary at all with the mesh density.

2.2.4 Nonlinear Computation Management

The use of a nonlinear adhesive material implies that the computation is nonlinear. A detailed description of the nonlinear algorithm used is provided in [24]. Only

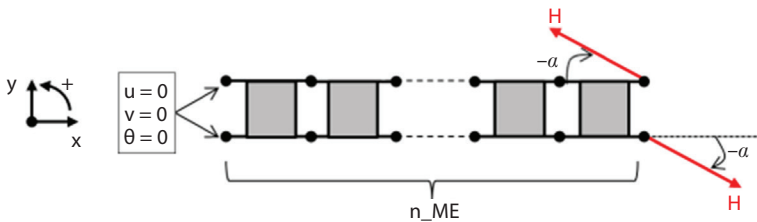


Figure 4 Applied displacement H and fixed displacement applied to an MCB test configuration.

a brief overview is given here. The algorithm is based on the Newton-Raphson method and uses the secant stiffness matrix with an update at each iteration. In particular, the damage parameter is computed at each nodal abscissa according to the introduced adhesive material law. The norm of displacement jump (in mm) of interface λ is defined by:

$$\lambda = \sqrt{(\delta_v)^2 + (\delta_u)^2} \quad (9)$$

where δ_v (δ_u) is the displacement jump of the interface (see Table 2) along the y-axis (x-axis). A mixity parameter β is defined by:

$$\beta = \frac{\delta_u}{\delta_v} = \frac{u_2 - u_1 - h_2 \theta_2 - h_1 \theta_1}{v_1 - v_2} \quad (10)$$

The mixity parameter is representative of the level of sliding displacement at the interface compared with the opening displacement at the interface. At each iteration, the mixity parameter β is updated. Under the current local mixity parameter, it is assumed that the material law is bilinear, such that the damage parameter d is:

$$d = \frac{\lambda_f (\lambda - \lambda_e)}{\lambda (\lambda - \lambda_f)} \quad (11)$$

where λ_e (λ_f) is the displacement jump (in mm) of the interface at initiation (propagation). In order to compute λ_e (λ_f), the interaction laws Eq. (1) are used while classically assuming that the projections on pure modes of the mixed mode evolution law under the current local mixity are bilinear (see Table 2):

$$\left\{ \begin{array}{l} \lambda_e = \delta_{ue} \delta_{ve} \sqrt{1 + \beta^2} \left[\frac{1}{(\delta_{ue})^{2n} + (\beta \delta_{ve})^{2n}} \right]^{\frac{1}{2n}} \\ \lambda_f = \delta_{uf} \delta_{vf} \sqrt{1 + \beta^2} \left[\frac{\sqrt{(\delta_{ue})^{2n} + (\beta \delta_{ve})^{2n}}}{(\delta_{ue} \delta_{uf})^n + (\beta^2 \delta_{ve} \delta_{vf})^n} \right]^{\frac{1}{n}} \end{array} \right. \quad (12)$$

The damage parameter is computed only if δ_v is positive. Each ME is then updated with the damaged elastic stiffness taken as the maximal value of both damage parameters computed at each extremity of the ME.

Finally, the displacement is linearly applied as a function of the numerical time. All the numerical test results presented in this paper are obtained from a simulation run involving one hundred time steps, with a constant numerical time step δ_t .

3 Characterization Method

3.1 The Inverse Method

The inverse method is based on the energy balance associated with the computation of the path independent J-integral [14] on a closed contour Γ :

$$J = \int W dy - \bar{T} \frac{d\bar{U}}{dx} ds \quad (13)$$

where W is the strain energy density, $\bar{T} = n\sigma$ is the traction vector, σ is the stress tensor, \bar{U} is the displacement vector, n is the normal unit vector directed outward to the path Γ , and (x,y) is the specified two-dimensional coordinate system. From the fundamental work by Fraise and Schmit [32] it is shown that the J-integral parameter can be computed from stress analysis based on a model of beam on an elastic foundation as:

$$J(\delta_u, \delta_v) = \int_0^{\delta_u} T(\delta_u, \delta_v) d\delta_u + \int_0^{\delta_v} S(\delta_u, \delta_v) d\delta_v \quad (14)$$

In the frame of the inverse method:

(i) the adhesive peel stress is obtained from experimental tests under pure mode I loading as [17]:

$$S(\delta_v) = \frac{\partial J(\delta_u, \delta_v)}{\partial \delta_v} \quad (15)$$

(ii) the adhesive shear stress is obtained from experimental tests under pure mode II loading as [15]:

$$T(\delta_u) = \frac{\partial J(\delta_u, \delta_v)}{\partial \delta_u} \quad (16)$$

(iii) the adhesive peel and shear stresses are obtained from experimental tests under mixed-mode I/II loading as [12–13]:

$$S(\delta_v) = \frac{\partial J(\delta_u, \delta_v)}{\partial \delta_v} \quad (17)$$

$$T(\delta_u) = \frac{\partial J(\delta_u, \delta_v)}{\partial \delta_u} \quad (18)$$

An advantage of this method is that it offers the possibility to monitor the evolution of the adhesive stress at the crack tip from the measurements of macroscopic quantities possibly measurable from experimental test fixtures, such as the

applied load (in N) or the evolution of displacement jump (in mm) at the crack tip. The related expressions can be found in [12–13, 15–20]. In order to address the constraints inherent to the numerical analysis (see section 2.2.3) the following approximate expression for the J-integral parameter, deduced from the work by Fraisse and Schmit [32] after the relevant adaptations to the Euler-Bernoulli framework (the same as ME) is used:

$$\begin{aligned}
 J(\delta_u, \delta_v) = & \frac{1}{2b} \left[\frac{N_1^2(L)}{A} + \frac{M_1^2(L)}{D} \right] + \frac{1}{2b} \left[\frac{N_2^2(L)}{A} + \frac{M_2^2(L)}{D} \right] - \\
 & \frac{1}{2b} \left[\frac{(N_1(0) + N_2(0))^2}{2A} + \frac{\left(M_1(0) + M_2(0) + \frac{h}{2}(N_2(0) - N_1(0)) \right)^2}{8D} \right] \quad (19) \\
 & + \frac{1}{b} [V_1(L) \theta_1(L) + V_2(L) \theta_2(L)] - \frac{1}{b} [V_1(0) \theta_1(0) + V_2(0) \theta_2(0)]
 \end{aligned}$$

This expression is valid when $A_1=A_2=A$, $D_1=D_2=D$, $B_1=B_2=0$ and $t_1=t_2=t=2h$. Even if the previous expression can be computed using the output from the stress analysis, it is nevertheless suitable for the analysis of experimental tests, which needs the application data reduction scheme [33–34]. In addition, the required differentiation of the J-integral parameter to obtain the adhesive peel and shear stresses at $x=L$ is taken as the ratio of the difference between two consecutive computed J over the difference between two consecutive computed displacement jump δ_u or δ_v :

$$\begin{cases}
 S(\delta_v(t)) = \frac{J(t) - J(t - \delta_t)}{\delta_v(t) - \delta_v(t - \delta_t)} \\
 T(\delta_u(t)) = \frac{J(t) - J(t - \delta_t)}{\delta_u(t) - \delta_u(t - \delta_t)}
 \end{cases} \quad (20)$$

This is the reason why the chosen numerical time step is elevated ($\delta_t = 100$).

3.2 The Direct Method

This method is presented in [21]. It is based on the measurement around the crack tip of the displacement of the neural axis according to the x-axis and the y-axis. Contrary to the inverse method, no spatial integration of equilibrium equations is required. It is assumed that the coupling stiffness remains equal to zero $B_1=B_2=0$;

the expressions for the adhesive shear stress including the coupling stiffnesses are provided in Appendix A.

In the case of pure mode I loading, the adhesive shear stress vanishes so that the local equilibrium of adherends can be reduced to the following set of differential equations for $j=1,2$:

$$\begin{cases} \frac{dN_j}{dx} = 0 \\ \frac{dV_j}{dx} = (-1)^{j+1} bS \\ \frac{dM_j}{dx} + V_j = 0 \end{cases} \quad (21)$$

As a result:

$$S = (-1)^j \frac{1}{b} \frac{d^2 M_j}{dx^2} \quad (22)$$

Using the constitutive relationship, the adhesive peel stress can be expressed as:

$$S = (-1)^j \frac{D_j}{b} \frac{d^4 w_j}{dx^4} \quad (23)$$

In the case of pure mode II loading, the adhesive peel stress vanishes so that the local equilibrium of adherends can be reduced to the following set of differential equations for $j = 1,2$:

$$\begin{cases} \frac{dN_j}{dx} = (-1)^j bT \\ \frac{dV_j}{dx} = 0 \\ \frac{dM_j}{dx} + V_j + bh_j T = 0 \end{cases} \quad (24)$$

As a result:

$$T = (-1)^j \frac{1}{b} \frac{dN_j}{dx} \quad (25)$$

Using the constitutive relationships, the adhesive shear stress can be expressed as:

$$T = (-1)^j \frac{A_j}{b} \frac{d^2 u_j}{dx^2} \quad (26)$$

In the case of mixed-mode I/II loading, the local equilibrium of adherends is given by Eq. (4). The following expressions for the adhesive peel and shear stresses are obtained:

$$S = (-1)^j \frac{D_j}{b} \frac{d^4 w_j}{dx^4} + h_j \frac{A_j}{b} \frac{d^3 u_j}{dx^3} \quad (27)$$

$$T = (-1)^j \frac{A_j}{b} \frac{d^2 u_j}{dx^2} \quad (28)$$

In the frame of this paper, the stress analysis provides the nodal displacements only, due to the approach chosen for the formulation of the elementary stiffness matrix. The consecutive differentiation of nodal displacements at the crack tip requires assessing the adhesive peel and shear stresses which are computed as the ratio of the difference between the displacements at the node located at $x=L$ and the node at $x=L-L/n_ME$ over $L-L/n_ME$.

3.3 Test Campaign

The assessment of both inverse and direct methods is performed through five different loading conditions, corresponding to five different values of the angle α (see Figure 4):

- i. pure mode I with $\alpha = \pi/2$;
- ii. mixed-mode I/II with $\alpha = \pi/4$;
- iii. mixed-mode I/II with $\alpha = \pi/8$;
- iv. mixed-mode I/II with $\alpha = \pi/16$;
- v. pure mode II with $\alpha = 0$.

For each of the five loading conditions, four virtual tests are performed and post-processed. Each of the virtual tests is associated with a mesh refinement or a density of mesh per mm:

- i. one ME per mm;
- ii. two MEs per mm;
- iii. four MEs per mm;
- iv. eight MEs per mm.

The results of the test campaign are presented and discussed in section 4. The results denoted as *theoretical* are related to the input data provided to the model

based on the constitutive behavior of the adhesive material. The results denoted as *computed* are related to direct output data of the numerical analysis as the adhesive stress distribution (using Eq. (3)), the reaction force or the J-integral parameter. Finally, results obtained from the inverse method and from the direct method are provided on the basis of computed results as described in section 3.1 and section 3.2 respectively. For each loading condition, the results are given up to the propagation beginning at $x=L$ (it means $d=1$ at $x=L$).

4 Results and Discussion

4.1 Pure Mode I and Pure Mode II

As a function of the displacement jump at $x=L$ and up to the propagation beginning at $x=L$ (it means $d=1$), the computed reaction forces F under pure mode I and pure mode II are provided for the four mesh densities in Figure 5 and Figure 6. It appears that the mesh density has a significant influence on the accuracy of predictions under pure mode I: a maximal relative difference of -11% in the reaction force is obtained for a mesh density of eight MEs per mm. The reaction force tends to stabilize with increase in mesh density. On the contrary, this influence appears as very limited under pure mode II, for the range of mesh density selected; a maximal relative difference of -1.1% in the reaction force is obtained for a mesh density of eight MEs per mm. However, the difference in the computed reaction forces with one ME per mm and eight MEs per mm remains similar for the pure mode I and pure mode II: 82 N and 84 N respectively. But the reaction force in pure mode II is about ten times higher than in pure mode I. As a result, the relative difference in pure mode II appears as much reduced.

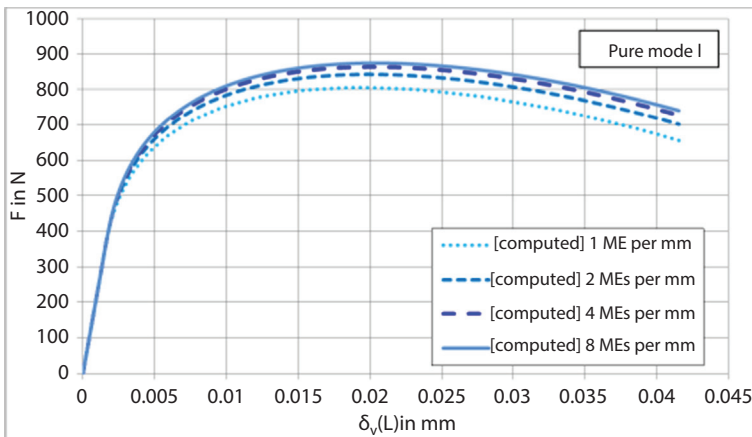


Figure 5 Reaction force as a function of the displacement jump at $x=L$ for the four mesh densities under mode I.

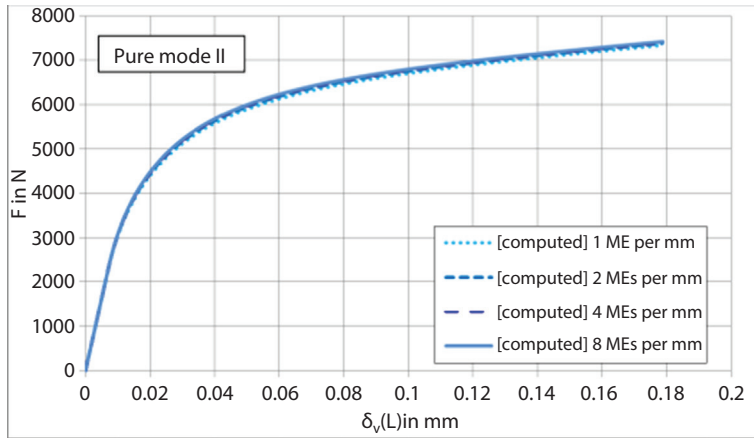


Figure 6 Reaction force as a function of the displacement jump at $x=L$ for the four mesh densities under mode II.

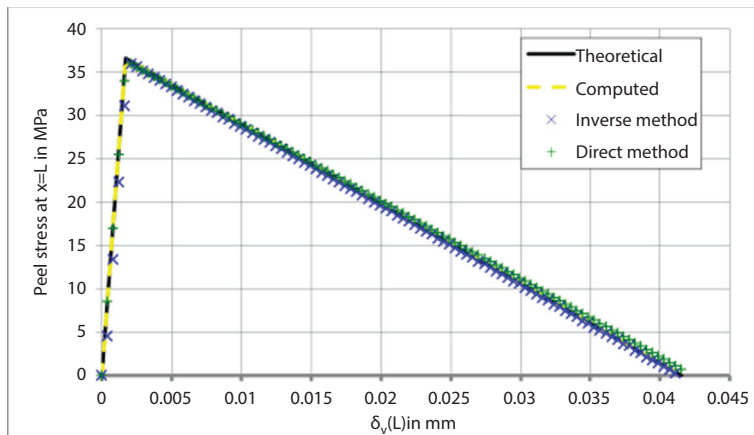


Figure 7 Peel stress at $x=L$ as a function of the displacement jump. Comparison of distributions among the theory, computation, the direct method and the inverse method for a mesh density of 8 MEs per mm.

The peel (shear) stress distributions as a function of the displacement jump at $x=L$ predicted by the inverse method and by the direct method are provided in Figure 7 (Figure 8) for a mesh density of eight MEs per mm. Moreover, they are compared with the theoretical and the computed ones. Under pure mode I, the four peel stress distributions appear as superimposed. Similarly, under pure mode II, the four shear stress distributions appear as very close. Only the inverse

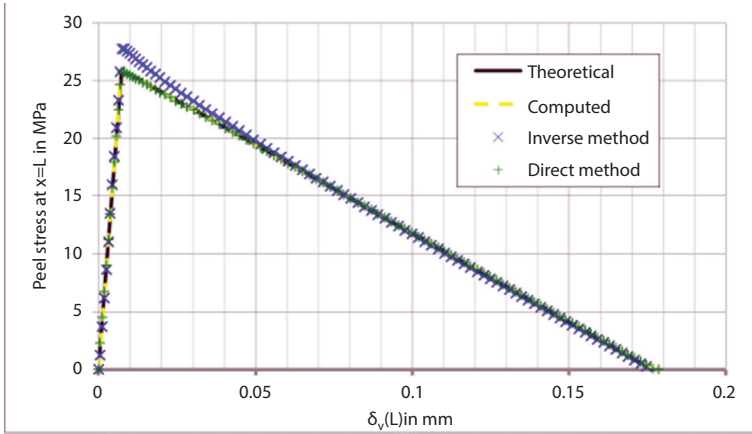


Figure 8 Shear stress at $x=L$ as a function of the displacement jump. Comparison of distributions among the theory, computation, the direct method and the inverse method for a mesh density of 8 MEs per mm.

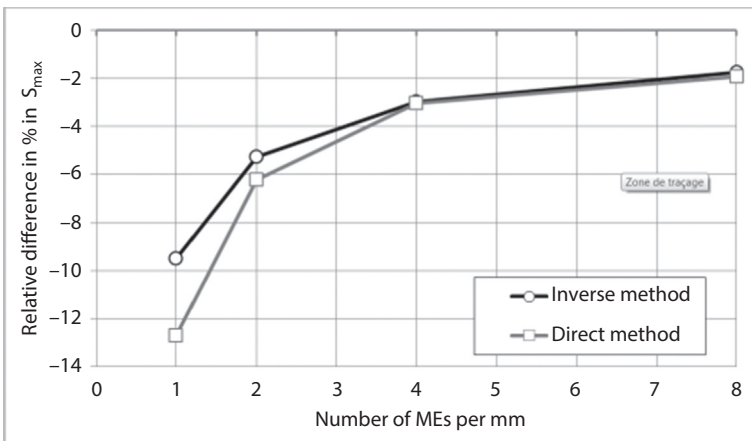


Figure 9 Relative difference in % in the maximal peel stress obtained with the inverse and direct methods from the theoretical peel stress peak as a function of mesh density.

method overestimates the maximal stress, before a slight underestimation at higher jump displacements. The relative differences in the maximal peel (shear) stresses obtained with the inverse and direct methods from the theoretical peel (shear) stress peaks are given in Figure 9 (Figure 10) as a function of the mesh density. Under pure mode I, the increase of mesh density tends to reduce the difference from the theoretical value for both methods and to reduce the rate of this

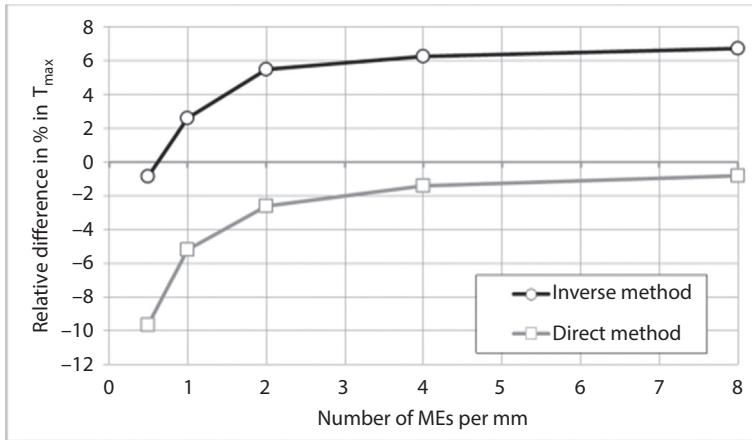


Figure 10 Relative difference in % in the maximal shear stress obtained with the inverse and direct methods from the theoretical shear stress peak as a function of mesh density.

evolution. This behaviour is observed for the direct method under pure mode II too. For the inverse method, if the increase in the mesh density reduces the evolution rate, the relative difference from the theoretical value tends to increase by up to 6.7%, which is not considered as significant.

It can be concluded firstly that the adhesive stress evolution computed as a function of displacement jump at $x=L$, referred to as the adhesive constitutive evolution, corresponds to the theoretical ones under pure mode I and pure mode II. Secondly, the direct method provides the theoretical adhesive constitutive evolution under pure mode I and pure mode II. Thirdly, if the inverse method provides the theoretical adhesive constitutive evolution under pure mode I, it provides under pure mode II a relevant adhesive constitutive evolution along the linear range and along a large part of the softening part of the constitutive behavior with possibly a slight overestimation of the maximal stresses. Nevertheless, from Figure 10, it is shown that the inverse method is able to predict the theoretical maximal stress, by selecting a coarser mesh density.

4.2 Mixed-Mode I/II

In this section, quadratic initiation and propagation criteria are used; this means $n=2$ in Eq. (1). The computed reaction forces F for the three mixed-mode loading conditions defined by $a = \pi/4$, $a = \pi/8$ and $a = \pi/16$ are provided as functions of the norm of the displacement jump of both interfaces at $x = L$ for the four mesh densities in Figure 11. Similarly to the pure mode II case, the influence of the mesh density on the computed reaction force appears as very limited, for the range selected, due to the increase of the level of the reaction force (see section 4.1). The reaction

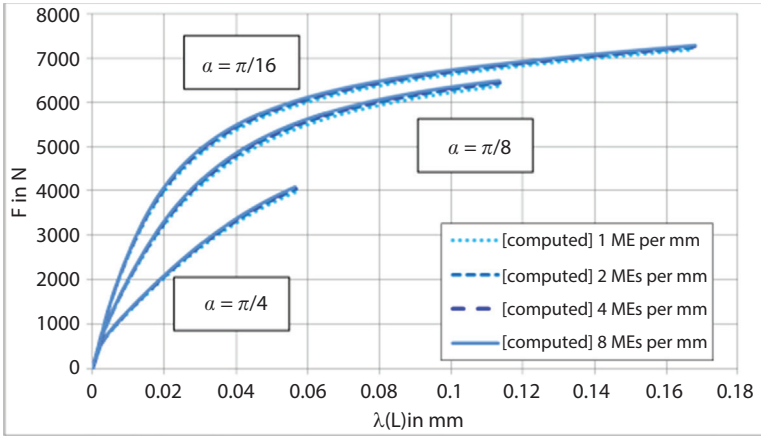


Figure 11 Reaction force as a function of the norm of displacement jump at $x=L$ for the four mesh densities under mixed-mode loading conditions $\alpha = \pi/4$, $\alpha = \pi/8$ and $\alpha = \pi/16$.

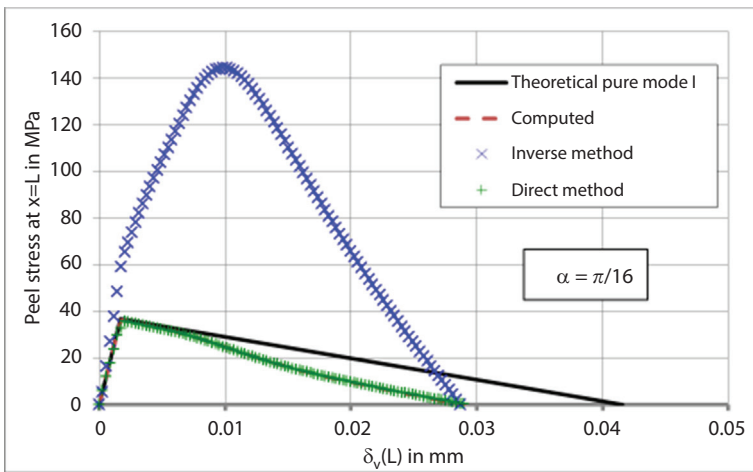


Figure 12 Peel stress at $x=L$ as a function of the displacement jump under a loading condition $\alpha = \pi/16$. Comparison of distributions among the theoretical pure mode I, computation, the direct method and the inverse method for a mesh density of 8 MEs per mm.

force computed for a mesh density of one ME per mm is different from the one for a mesh density of eight MEs per mm, i.e., -2.4% , -1.8% and -1.2% for $\alpha=\pi/4$, $\alpha=\pi/8$ and $\alpha = \pi/16$, respectively.

The adhesive peel and shear stress distributions as a function of the displacement jump at $x = L$ predicted by the inverse method and by the direct method are provided in Figure 12 and Figure 13 respectively, for a mesh density of eight

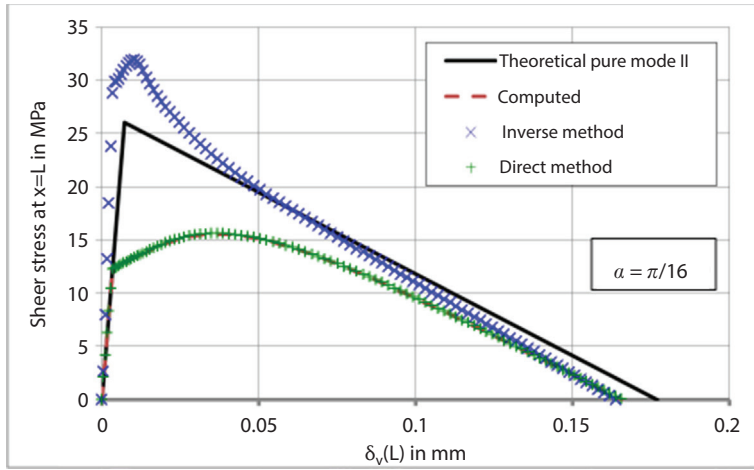


Figure 13 Shear stress at $x = L$ as a function of the displacement jump under a loading condition $\alpha = \pi/16$. Comparison of distributions among the theoretical pure mode II, computation, the direct method and the inverse method for a mesh density of 8 MEs per mm.

MEs per mm and under a loading condition $\alpha = \pi/16$. Moreover, the pure mode evolutions are also shown in the figures.

It is shown that the predictions by the direct method and the inverse method are different. Of course, the direct method predicts the computed results, since the direct method and the numerical simulations based on ME use the same hypotheses. The accuracy of direct method predictions is related to the post-processing approach and thus to the mesh refinement (see Figure 14). The adhesive constitutive evolutions in peel and in shear under mixed-mode identified by the inverse method are significantly different from the computed ones. The reason is that the way the shear and peel stresses are obtained in the inverse method under mixed-mode are not mathematically true in general. Indeed, Eq. (14) does not lead to Eq. (17) and Eq. (18) in general. The particular CZM used in this paper to model the behaviour of the adhesive layer in the bonded joint is thus a case for which it is not true. When it is true, the adhesive peel and shear stresses are derivable from a potential energy [35]. For the particular CZM used in this paper, the adhesive peel and shear stresses appear as not derivable from a potential energy so that the work of separation is path-dependent.

Moreover, the constitutive adhesive evolutions in peel and shear computed and predicted by the direct method are given for a mesh density of eight MEs per mm and for the three loading conditions in Figure 15 and Figure 16 respectively. Under the mixed-mode loading conditions $\alpha = 11\pi/4$ and $\alpha = \pi/8$, the adhesive constitutive evolution in peel remains very close to the pure mode I (see Figure 15): with no

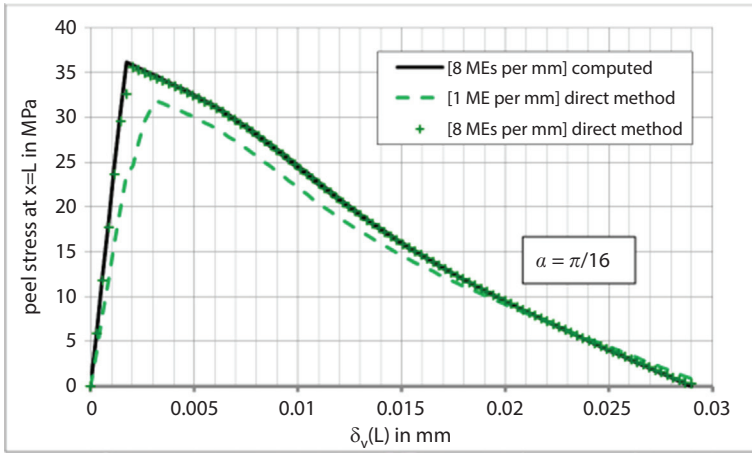


Figure 14 Peel stress computed from the direct method at $x = L$ as a function of the displacement jump under a loading condition $\alpha = \pi/16$ for 1 ME per mm and 8 MEs per mm.

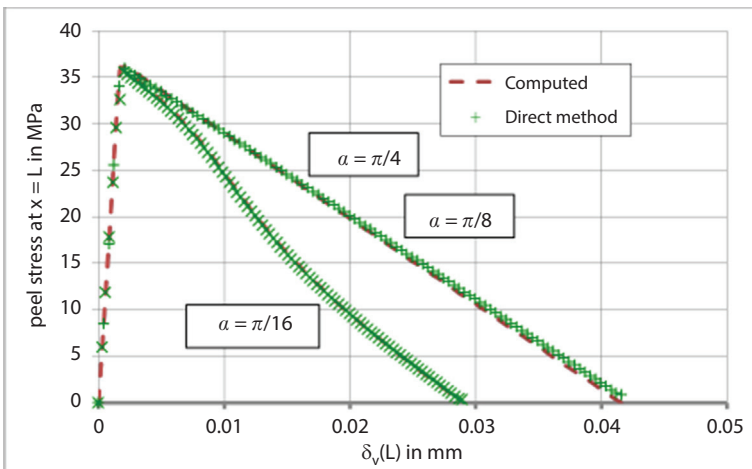


Figure 15 Peel stress at $x=L$ as a function of the displacement jump for the three mixed-mode loading conditions.

more than a small difference of -1.7% from the maximal theoretical peel stress. On the contrary, the variation in mixed-mode loading conditions is clearly shown in the adhesive constitutive evolution in shear (see Figure 16). It can thus be deduced that loading conditions close to the pure mode II are relevant choices for the experimental characterization of the mechanical behavior of the adhesive layer under mixed-mode loading conditions, if the MCB test configuration is chosen.

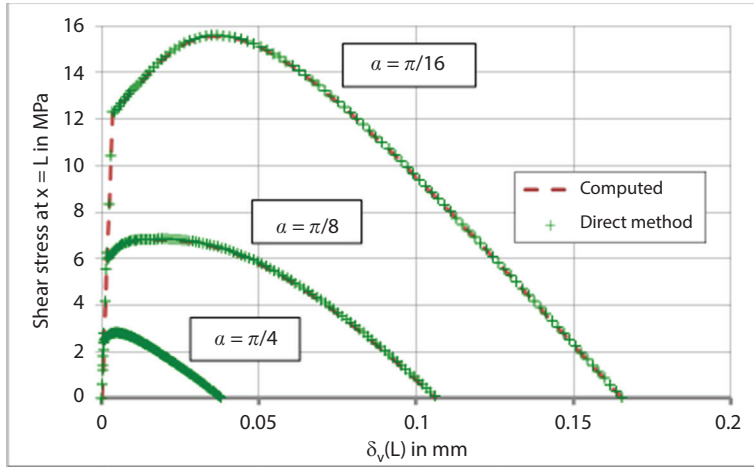


Figure 16 Shear stress at $x=L$ as a function of the displacement jump for the three mixed-mode loading conditions.

The actual level of mixity at $x=L$ has been investigated. A local mixity angle ψ relevant to the actual description of loading conditions (angle α) is defined as:

$$\psi = \frac{\pi}{2} - \tan^{-1} \beta \quad (29)$$

As already shown in [13], the local mixity angle at $x=L$ differs from the loading condition α for the crack length selected (see Figure 17). Moreover, as a function of the increase of the damage parameter at $x=L$, the local mixity angle at $x=L$ decreases to reach a value close to α . This evolution of the local mixity angle should lead to the shapes of the peel and shear stresses (see Figure 15 and Figure 16) which deviate from those of pure mode ones.

4.3 Assessment of Mixed-Mode I/II Criterion

There are several shapes of initiation and propagation [10–11, 21, 36]. An approach could consist in choosing a shape for the initiation and propagation and then to best fit the related parameters to the assessed peel and shear stresses. The energy criterion for initiation and propagation in this paper uses only one material parameter, the exponent n (see Eq. (1)). A comparison of the reaction force, adhesive peel and shear stress as a function of jump displacement is then provided between $n=1$ and $n=2$ in Figure 18 to Figure 20. The loading condition $\alpha=\pi/16$ and a mesh density of eight MEs per mm are chosen. When the damage propagates at $x=L$, the reaction force computed with $n=1$ shows a relative difference of -4.9% from

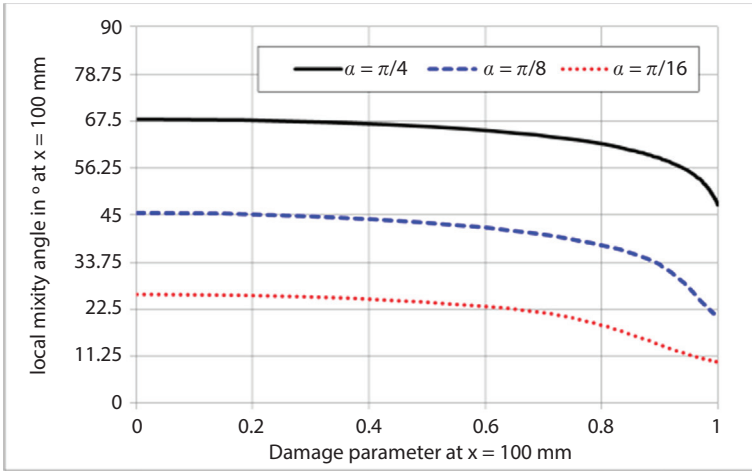


Figure 17 Local mixity angle at $x = L$ as a function of the damage parameter at $x = L$.

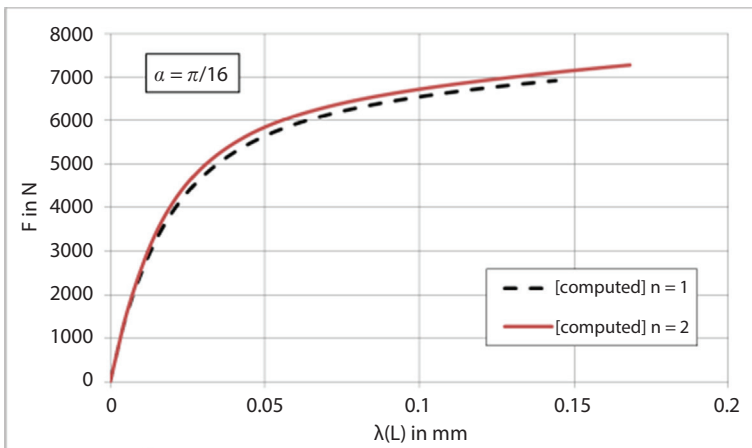


Figure 18 Computed reaction force as a function of the displacement jump under mixed-mode loading condition $\alpha = \pi/16$ for $n = 1$ and $n = 2$ with a mesh density of eight MEs per mm.

the one with $n=2$. As a result, a small difference is thus shown on the macroscopic measurement due to the choice of the mixed-mode model. Qualitatively, the shape of the adhesive constitutive evolution in peel and shear is similar for $n=1$ and $n=2$, although a slight variation in the slopes after the initiation is observed. Nevertheless, a clear difference appears quantitatively in terms of level of stress and jump displacement. A relative difference of -10% (-17%) for the case with $n=2$

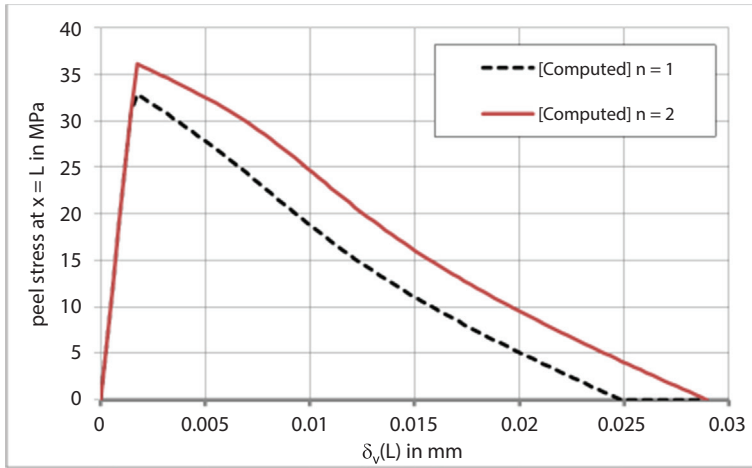


Figure 19 Computed peel stress at $x = L$ as a function of the displacement jump under mixed-mode loading condition $\alpha = \pi/16$ for $n = 1$ and $n = 2$ with a mesh density of eight MEs per mm.

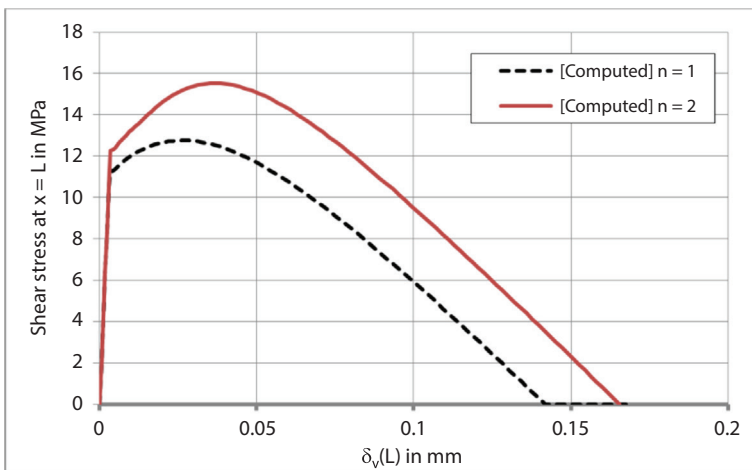


Figure 20 Computed shear stress at $x = L$ as a function of the displacement jump under mixed-mode loading condition $\alpha = \pi/16$ for $n = 1$ and $n = 2$ with a mesh density of eight MEs per mm.

is obtained for the maximal peel (shear) stress, respectively. As a result, it could be thought that models for the initiation and propagation could be assessed through the use of both the direct method and the numerical analysis. Finally, since the inverse method cannot always be used under mixed mode loading, it could be

thought that the assessment provided by the direct method could be restricted to a particular combination of geometrical parameters, material parameters and boundary conditions under consideration.

5 Summary and Conclusions

In order to identify the parameters of CZM for thin adhesive layers, the inverse method and the direct method have been tested through a numerical test campaign. The numerical test campaign is based on the ME technique. A new approach for a fast formulation of the elementary stiffness matrix of bonded-beams element is provided in this paper. It can be concluded firstly that both inverse method and direct method are able to predict the adhesive constitutive evolution in both pure modes I and II. Secondly, the direct method provides accurate predictions under mixed-mode loading conditions. Thirdly, the inverse method fails in the assessment of the adhesive shear and peel stresses as a function of displacement jump under mixed-mode loading, with the particular CZM (but having a classical shape) used in this paper to model the adhesive layer in the bonded overlap. The use of the inverse method should then be restricted to the assessment of the adhesive constitutive evolution under pure modes only. Considering the J-integral framework, other restrictions should be considered when using the inverse method such as loading and unloading scheme or material time-dependent characteristics. Although the direct method appears as attractive, it could be difficult to apply in practice. Indeed, third-order and fourth-order differentiations of measured displacements are required, so dedicated methods to process the recorded signals should be employed. Under pure mode I and pure mode II, the order of differentiation could be reduced if the strain field on the external skin of adherends is recorded [3]. From [37], it is clear that the experimental measurement of values such as applied force as a function of displacement jump is not sufficient for an accurate assessment of debonding problems. Nevertheless, assuming that the practical means are available to post-process the experimental test results for a reliable assessment of successive differentiations of measured displacements, the direct method would offer the possibility to investigate the CZM for thin adhesive layers. In particular, the experimental characterization of the shapes of constitutive adhesive evolutions under pure mode I, pure mode II and mixed-mode I/II could lead to validate the CZM available in the literature or to develop other ones by changing some of the underlying hypotheses. For this objective, the shape of the constitutive adhesive stress is of highest interest. That is why the authors of this paper are currently investigating this topic. The use of a novel experimental test technique [38] allowing for the application of a wide range of mixed-mode ratios could be considered in conjunction with the direct method. It is indicated that the use of a series of loading and unloading schemes could help in a refined *understanding* of the mechanical behaviour of thin adhesive layers. Finally, when an adhesive layer needs to be characterized, its material behaviour is unknown



a priori. As a result, a preliminary and iterative step including experimental and numerical tests has to be conducted to design the test specimen to demonstrate the ability to obtain relevant experimental data. The use of the ME technique could help in reducing the computation time for numerical tests to virtually explore the design possibilities associated with the loading conditions geometries and adhesive constitutive behaviour laws. The implementation of an ME using the Timoshenko model instead of Euler-Bernoulli model could improve the relevance of the assessment of constitutive laws, especially when using thicker adherends.

Acknowledgement

The author affiliated to Sogeti High Tech gratefully acknowledges the engineers and the managers involved in the development of JoSAT (Joint Stress Analysis Tool), which is an internal research program. Both first authors indicate that this paper is a contribution to the initiative TACCOS; TACCOS stands for "Toulouse Adh sion Coh sion Collage Structural, de la Chimie   la M canique" which means "Toulouse Adhesion Cohesion Structural Adhesive Bonding, from Chemistry to Mechanics" in English.

Appendix A

The expressions for the adhesive peel and shear stresses including the coupling stiffnesses are obtained as explained in section 3.2 by using the constitutive equations of adherends (Eq. (2)) and the local equilibrium equations of adherends (Eq. (4)).

Under pure mode I, the adhesive shear stress vanishes, so that:

$$S = (-1)^j \left[-\frac{B_j}{b} \frac{d^3 u_j}{dx^3} + \frac{D_j}{b} \frac{d^4 w_j}{dx^4} \right] \quad (\text{A-1})$$

Under pure mode II, the adhesive peel stress vanishes, so that:

$$T = (-1)^j \left[\frac{A_j}{b} \frac{d^2 u_j}{dx^2} - \frac{B_j}{b} \frac{d^3 w_j}{dx^3} \right] \quad (\text{A-2})$$

Under pure mixed-mode I/II, the adhesive peel and shear stresses are given by:

$$S = \left[(-1)^j \frac{D_j}{b} - h_j \frac{B_j}{b} \right] \frac{d^4 w_j}{dx^4} + \left[h_j \frac{A_j}{b} - (-1)^j \frac{B_j}{b} \right] \frac{d^3 u_j}{dx^3} \quad (\text{A-3})$$

$$T = (-1)^j \left[\frac{A_j}{b} \frac{d^2 u_j}{dx^2} - \frac{B_j}{b} \frac{d^3 w_j}{dx^3} \right] \quad (\text{A-4})$$

Nomenclature and Units

A_j	extensional stiffness (N) of adherend j
B_j	extensional and bending coupling stiffness (N.mm) of adherend j
D_j	bending stiffness (N.mm ²) of adherend j
E^j	adherend Young's modulus (MPa)
F	magnitude of applied force (N)
G_I	strain energy release rate (energy per unit area: mJ or N/mm) in peel
G_{II}	strain energy release rate (energy per unit area: mJ or N/mm) in shear
G_{Ic}	adhesive fracture energy (energy per unit area: mJ or N/mm) in peel
G_{Ie}	adhesive elastic strain energy stored (energy per unit area: mJ or N/mm) in peel
G_{IIc}	adhesive fracture energy (energy per unit area: mJ or N/mm) in shear
G_{IIe}	adhesive elastic strain energy stored (energy unit area: mJ or N/mm) in shear
H	magnitude of applied displacement (mm)
J	J-integral parameter
K_{BBe}	elementary stiffness matrix of a bonded-beam element
L	length (mm) of bonded overlap
M_j	bending moment (N.mm) in adherend j around the z direction
N_j	normal force (N) in adherend j in the x direction
S	adhesive peel stress (MPa)
S_{max}	maximal adhesive peel stress (MPa)
T	adhesive shear stress (MPa)
T_{max}	maximal adhesive shear stress (MPa)
V_j	shear force (N) in adherend j in the y direction
a	crack length (mm)
b	width (mm) of the adherends
d	damage parameter
e	thickness (mm) of the adhesive layer
h_j	half thickness (mm) of adherend j
k_I	adhesive elastic stiffness (MPa/mm) in peel
k_{II}	adhesive elastic stiffness (MPa/mm) in shear
n	power used in the adhesive material law
n_{ME}	number of macro-elements
t	adherend thickness (mm)
u_j	displacement (mm) of adherend j in the x direction
v_j	displacement (mm) of adherend j in the y direction
Δ	overlap length (mm) of a macro-element
Δ_j	characteristic parameter of adherend j in N ² .mm ²
α	angle (rad) used for the definition of the load application in MCB test
β	mixed-mode parameter
δ_t	numerical time step (s)

δ^u	displacement jump (mm) of the interface along the x-axis
δ^{ue}	displacement jump (mm) of the interface along the x-axis at initiation
δ^{uf}	displacement jump (mm) of the interface along the x-axis at propagation
δ^v	displacement jump (mm) of the interface along the y-axis
δ^{ve}	displacement jump (mm) of the interface along the y-axis at initiation
δ^{vf}	displacement jump (mm) of the interface along the y-axis at propagation
λ	norm of displacement jump (mm) of the interface
λ_e	norm of displacement jump (mm) of the interface at initiation
λ_f	norm of displacement jump (mm) of the interface at propagation
ν	adherend Poisson's ratio
θ_j	bending angle (rad) of the adherend j around the z direction
ψ	local mixity angle (rad)
(x,y,z)	system of axes
CZM	cohesive zone model
DCB	double cantilever beam
ENF	end notched flexure
FE	Finite Element
MCB	mixed mode cantilever beam
ME	macro-element

References

1. L.J. Hart-Smith, Design methodology for bonded-bolted composite joints, Technical Report, AFWAL-TR-81-3154, Douglas Aircraft Company, Long Beach, California (1982).
2. G. Kelly, Quasi-static strength and fatigue life of hybrid (bonded/bolted) composite single-lap joints. *J. Composite Struct.* **72**, 119–129 (2006).
3. J. Jumel, M.K. Budzik, N. Ben Salem, and M.E.R. Shanahan, Instrumented end notched flexure – Crack propagation and process zone monitoring. Part I: Modelling and analysis. *Int. J. Adhesion Adhesives* **50**, 297–309 (2013).
4. H. Khoramishad, A.D. Crocombe, K.B. Katnam, and I.A. Ashcroft, A generalized damage model for constant amplitude fatigue loading of adhesively bonded joints. *Int. J. Adhesion Adhesives* **30**, 513–521 (2010).
5. H. Khoramishad, A.D. Crocombe, K.B. Katnam, and I.A. Ashcroft, Fatigue damage modeling of adhesively bonded joints under variable amplitude loading using cohesive zone model. *Eng. Fracture Mech.* **78**, 3212–3225 (2011).
6. S. Li, M.D. Thouless, A.M. Waas, J.A. Schroeder, and P.D. Zavattieri, Mixed-mode cohesive zone models for fracture of an adhesively bonded polymer matrix composite. *Eng. Fracture Mech.* **73**, 64–78 (2006).
7. L.F.M. da Silva and R.D.S.G. Campilho, Advances in numerical modeling of adhesive joints, Springer Briefs in Computational Mechanics (2012). DOI: 10.1007/978-642-23608_1
8. R.D.S.G. Campilho, M.D. Banea, J.A.B.P. Neto, and L.F.M. da Silva, Modelling adhesive joints with cohesive zone models: Effects of the cohesive law shape of the adhesive layer. *Int. J. Adhesion Adhesives* **44**, 48–56 (2013).

9. H. Hadavinia, A.J. Kinloch, M.S.G. Little, A.C. Taylor, and J.R. Crews, The prediction of crack growth in bonded joints under cyclic-fatigue loading II. Analytical and finite element studies. *Int. J. Adhesion Adhesives* **23**, 463–471 (2003).
10. J.R. Reeder and J.R. Crews, Mixed-mode bending method for delamination testing. *AIAA J.* **28**, 1270–1276 (1990).
11. M. Kenane and M.L. Benzeggagh, Mixed-mode delamination fracture toughness of unidirectional glass/epoxy composites under fatigue loading. *Composites Sci. Technol.* **57**, 597–605 (1997).
12. J.L. Högberg, Mixed-mode testing of adhesive layer, in Proc. 27th International Symposium on Materials Science, Polymer Composite Materials for Wind Power Turbines, Risø, Denmark (2006).
13. J.L. Högberg and U. Stigh, Specimen proposals for mixed-mode testing of adhesive layer. *Eng. Fracture Mech.* **73**, 2541–2556 (2007).
14. J.R. Rice, A path independent integral and the approximate analysis of strain concentration by notches and cracks. *J. Appl. Mech.* **35**, 379–386 (1968).
15. K.S. Alfredsson, A. Biel, and K. Leffler, An experimental method to determine the complete stress-deformation relation for a structural adhesive layer loaded in shear, in Proc 9th International Conference on The Mechanical Behavior of Materials, Geneva (2003).
16. K.S. Alfredsson, On the instantaneous energy release rate of the end notched flexure adhesive joint specimen. *Int. J. Solids Struct.* **41**, 4787–4807 (2004).
17. T. Anderson and U. Stigh, The stress-elongation relation for an adhesive loaded in peel using equilibrium of energetic forces. *Int. J. Solids Struct.* **41**, 413–434 (2004).
18. K. Leffler, K.S. Alfredsson, and U. Stigh, Shear behavior of adhesive layers. *Int. J. Solids Struct.* **44**, 530–545 (2007).
19. H. Cui H, S. Koussios, Y. Li, and A. Beukers, Constitutive law of adhesive layer measured with mixed-mode bending test. *Eng. Fracture Mech.* **127**, 235–251 (2014).
20. H. Cui, Delamination and debonding failure of laminated composite T-joints, PhD Thesis, Delft University of Technology, Delft, The Netherlands (2014).
21. G. Lélías, Mechanical behavior of adhesively bonded joints: Modeling, simulation and experimental characterization, PhD Thesis, University of Toulouse 3, Toulouse, France (2016).
22. E. Paroissien, M. Sartor, J. Huet, and F. Lachaud, Analytical two-dimensional model of a hybrid (bolted/bonded) single-lap joint. *J. Aircraft* **44**, 573–582 (2007).
23. E. Paroissien, F. Lachaud, and T. Jacobs, A simplified stress analysis of bonded joints using macro-elements, in *Advances in Modeling and Design of Adhesively Bonded Systems*, S. Kumar and K.L. Mittal (Eds), pp. 93–146, Wiley-Scrivener, Beverly, Massachusetts (2013).
24. G. Lélías, E. Paroissien, F. Lachaud, J. Morlier, S. Schwartz, and C. Gavaille, An extended semi-analytical formulation for fast and reliable mode I/II stress analysis of adhesively bonded joints. *Int. J. Solids Struct.* **62**, 18–38 (2015).
25. O. Allix and P. Ladevèze, Damage mechanics of interfacial media: Basic aspects, identification and application to delamination, in *Damage and Interfacial Debonding in Composites*, Studies in Applied Mechanics 44, D. Allen and G. Voyiadjis (Eds.), pp. 167–88, Elsevier (1996).
26. A. Turon, P.P. Camanho, J. Costa, and J. Renart, Accurate simulation of delamination growth under mixed-mode loading using cohesive elements: Definition of interlaminar strengths and elastic stiffness. *Composite Struct.* **92**, 1857–1864 (2010).



27. E. Paroissien, F. Lachaud, S. Schwartz, A. Da Veiga, and P. Barrière, Simplified stress analysis of hybrid (bolted/bonded) joints. *Int. J. Adhesion Adhesives* **77**, 183–197 (2017).
28. M. Goland and E. Reissner, The stresses in cemented joints. *J. Appl. Mech.* **11**, A17–A27 (1944).
29. L.J. Hart-Smith, Adhesive bonded single lap joints, NASA Technical Report, CR-112236, Douglas Aircraft Company, Long Beach, California (1973).
30. Q. Luo and L. Tong, Analytical solutions for nonlinear analysis of composite single-lap joints. *Int. J. Adhesion Adhesives* **29**, 144–154 (2009).
31. M.Y. Tsai, D.W. Oplinger, and J. Morton, Improved theoretical solutions for adhesive lap joints. *Int. J. Solids Struct.* **35**, 1163–1185 (1998).
32. P. Fraise and F. Schmit, Use of J-integral as fracture parameter in simplified analysis of bonded joints. *Int. J. Fracture* **63**, 59–73 (1993).
33. C. Sarrado, J. Turon, J. Renart, and J. Costa, An experimental data reduction method for the mixed mode bending test based on the J-integral approach, *Composites Sci. Technol.* **117**, 85–91 (2015).
34. S. Azari, L. Eskandarian, M. Papini, J.A. Schroeder, and J.K. Spelt, Fracture load predictions and measurements for toughened epoxy adhesive joints. *Eng. Fracture Mech.* **76**, 2039–2055 (2009).
35. S. Goustianos and B.F. Sørensen, Path dependence of truss-like mixed mode cohesive laws. *Eng. Fracture Mech.* **91**, 117–132 (2012).
36. N. Valoroso and L. Champaney, A damage model for simulating decohesion in adhesively bonded assemblies, in: Proc. European Congress on Computational Methods in Applied Sciences and Engineering, Jyväskylä, Finland (2004).
37. G. Alfano, On the influence of the shape of the interface law on the application of cohesive-zone models. *Composites Sci. Technol.* **66**, 723–730 (2006).
38. M. Costa, R. Carbas, M. Benedita, E. Marques, L.F.M. da Silva, E. Yokoi, S. Nakada, and T. Furusawa, Static assessment of the mixed-mode behavior of three epoxy adhesives. *Eng. Fracture Mech.* **182**, 552–565 (2017).